

First return maps for the dynamics of synaptically coupled conditional bursters

Evandro Manica · Georgi S. Medvedev ·
Jonathan E. Rubin

Received: 13 January 2010 / Accepted: 16 June 2010 / Published online: 8 July 2010
© Springer-Verlag 2010

Abstract The pre-Bötzinger complex (preBötC) in the mammalian brainstem has an important role in generating respiratory rhythms. An influential differential equation model for the activity of individual neurons in the preBötC yields transitions from quiescence to bursting to tonic spiking as a parameter is varied. Further, past work has established that bursting dynamics can arise from a pair of tonic model cells coupled with synaptic excitation. In this paper, we analytically derive one- and two-dimensional maps from the differential equations for a self-coupled neuron and a two-neuron network, respectively. Using a combination of analysis and simulations of these maps, we explore the possible forms of dynamics that the model networks can produce as well as which transitions between dynamic regimes are mathematically possible.

Keywords Maps · Bursting · Synaptic coupling · Pre-Bötzinger complex

E. Manica
Departamento de Matematica, Universidade Federal do Rio Grande do Sul, Porte Alegre, RS, CEP 91509-900, Brazil
e-mail: evandro.manica@ufrgs.br

G. S. Medvedev
Department of Mathematics, Drexel University, Philadelphia, PA, 19104, USA
e-mail: medvedev@drexel.edu

J. E. Rubin (✉)
Department of Mathematics and Center for the Neural Basis of Cognition, University of Pittsburgh, Pittsburgh, PA, 15260, USA
e-mail: rubin@math.pitt.edu

1 Introduction

Biology provides many examples of systems where individual units, such as organisms, cells, or molecules, display qualitatively different dynamics under different conditions. Particular dynamic regimes often have specific functional consequences, and hence the conditions under which each form of dynamics appears, and the mechanisms underlying transitions between dynamic regimes, represent important topics for analysis in models of biological systems. Square-wave, or fold-homoclinic, bursting is a relatively complex activity pattern (Rinzel 1985; Izhikevich 2000) that arises in mathematical models for a variety of biological systems, including pancreatic β -cells (Chay and Keizer 1983) and neurons in a respiratory region of the mammalian brain stem, the pre-Bötzinger complex (preBötC) (Smith et al. 1991; Butera et al. 1999a; Best et al. 2005). For some time now, the minimal mathematical ingredients needed for square-wave bursting to arise in a single model cell and the mechanisms by which such a cell can switch its behavior between quiescence, square-wave bursting, and another form of activity, called tonic spiking, have been understood (Rinzel 1985; Terman 1992). Chaotic activity within transitional regions has also been analyzed (Terman 1991; Medvedev and Yoo 2008). However, although the burst-capable cells in the relevant biological systems belong to coupled networks, the analysis of transitions between dynamic regimes in model coupled networks has been relatively limited. The main point of this work is to develop a reduced representation, based on return maps, for a coupled pair of burst-capable model preBötC cells (Butera et al. 1999a,b) and to show how different activity patterns, and transitions between them, arise in the map representation.

To do so, we build heavily on two earlier papers, in addition to the two papers (Butera et al. 1999a,b) that first

introduced the model that we consider. In the study of a variety of models used in neuroscience (Ermentrout and Kopell 1998; LoFaro and Kopell 1999; Channell Jr. et al. 2007), and in other areas as well (Gomes et al. 2008; Altendorfer et al. 2003; Ditto et al. 1990; Milik et al. 1998; Rinzel and Troy 1982a,b), high dimensional systems of differential equations have been reduced to one-dimensional maps to facilitate analysis. Maps have also been constructed phenomenologically to reproduce some important characteristics of a given activity pattern (Wang 1991; Rulkov 2002, 2004). In this work, we follow a rigorous reduction, derived recently by Medvedev (2005) for individual square-wave burst-capable elements such as the single-cell Butera et al. (1999a) preBötC model, that takes advantage of the presence of two disparate timescales in the model. We recapitulate Medvedev's approach to show explicitly how it plays out for a self-coupled model preBötC cell. Further, we provide a novel extension of the reduction to the case of a pair of model cells, mutually coupled with synaptic excitation, which yields a two-dimensional map.

Second, in our analysis of the two-dimensional map, we make extensive comparison with another recent study of the dynamics of a pair of coupled model preBötC cells (Best et al. 2005). In that work, numerical simulation and bifurcation analysis of an appropriate slow averaged system revealed the existence of four different dynamic regimes and explained the mathematical mechanisms underlying transitions between these regimes, in the singular limit where a fast-slow decomposition applies. Here, we show how each dynamic regime is manifested in the two-dimensional map and arrive at a more comprehensive representation of possible transitions between regimes, valid when the ratio of the slow and fast timescales is small, but not necessarily zero as in the singular limit.

The paper is organized as follows. In Sect. 2, we present the version of the differential equation model that we study. For this model, we review the dynamic mechanisms that give rise to bursting in a single cell and in a two-cell network. In Sect. 3, we consider the one-dimensional map derived from the single cell equations, properties of this map, and constraints on the possible forms of single cell dynamics that can be inferred from the map. Section 4 presents similar topics for the two-dimensional map description of a two-cell network. In particular, we introduce an iterated map approach that we find useful for the study of this map. Section 5 provides a brief discussion of our results, while Appendix A gives further details of functions and parameter values used in the model, and Appendix B presents analytical arguments underlying some of the mathematical properties of the one-dimensional map. We note that, although we present our analysis in terms of the Butera et al. preBötC model, our qualitative results generalize immediately to any other model that shares its timescale decomposition and bifurcation structure.

2 Model and previous results

The original Butera et al. model describes the time (t) evolution of the membrane potential (v), activation (n), and inactivation (h) levels associated with certain transmembrane currents, and fraction (s) of maximal synaptic conductance available, for a single preBötC cell (Butera et al. 1999a). For completeness, this model is presented in Appendix A. In this paper, we work with the following version of the Butera et al. preBötC model (Butera et al. 1999a), rescaled such that voltage lies in $(-1, 1)$ and cast in a way that allows for consideration of either one or two cells:

$$\frac{dV_i}{dT} = (-I_{\text{NaP}}(V_i, h_i) - I_{\text{Na}}(V_i, n_i) - I_{\text{K}}(V_i, n_i) - I_{\text{L}}(V_i) - I_{\text{ton}}(V_i) - I_{\text{syn}}(V_i))/\rho \equiv F(V_i, h_i, n_i) \quad (1)$$

$$\frac{dh_i}{dT} = \epsilon(h_{\infty}(V_i) - h_i)/\tau_h^*(V_i) \quad (2)$$

$$\frac{dn_i}{dT} = (n_{\infty}(V_i) - n_i)/\tau_n^*(V_i) \quad (3)$$

$$\frac{ds_i}{dT} = \alpha_s(1 - s_i)s_{\infty}(V_j) - s_i/\tau_s, \quad (4)$$

where a standard approximation is used to incorporate the variable n_i into both the fast sodium and potassium currents, $I_{\text{Na}} = g_{\text{Na}}m_{\infty}^3(V_i)(1 - n_i)(V_i - E_{\text{Na}}^*)$ and $I_{\text{K}} = g_{\text{K}}n_i^4(V_i - E_{\text{K}}^*)$. In the self-coupled case, $i = j = 1$, while in the two-cell case, $i = 1, 2$ and $j = 3 - i$. This system is obtained from the original model by rescaling variables for time ($T = t/10$ for t from the original model in Appendix A) and voltage ($v = 100V$), as well as maximal conductances ($g_i = \frac{\bar{g}_i}{g_{\text{Na}}}$) and reversal potentials ($E_i^* = E_i/100$), and introducing the new parameters

$$\rho = C_m/(10\bar{g}_{\text{Na}}) = 7.5 \times 10^{-2}, \quad \epsilon = 10^{-3}, \quad \alpha_s = 2, \\ \tau_s = \bar{\tau}_s/10 = 0.5,$$

where parameters with bars on them are from the original Butera model. We have also introduced the rescaled, voltage-dependent timescale functions

$$\tau_h^*(V_i) = \sec h[(V_i + 0.48)/0.12]$$

and

$$\tau_n^*(V_i) = \sec h[(V_i + 0.29)/(-0.08)].$$

Note, in particular, that we have factored out the small parameter ϵ from Eq. 2. For unscaled voltages, v , between -80 and 10 mV, the quantity $\epsilon/\tau_h(V)$ remains below 0.07 , while $1/\tau_n(V)$ is always above 1 and is well above 1 over most of this range. Moreover, $h_{\infty}(V_i), n_{\infty}(V_i) \in (0, 1)$ for each i , such that $h_i, n_i \in (0, 1)$ as well. Hence, we treat h_i as slow relative to the other variables in the system. The nature of the rescaling implies that system (1–4) has the same dynamics and associated structures as the original model. In

the rest of this section, we summarize the key features of system (1–4).

2.1 Single-cell dynamics

Since h_i is slow, it is natural to define the fast or inner subsystem

$$\begin{aligned} V_i' &= F(V_i, h_i, n_i) \\ n_i' &= (n_\infty(V_i) - n_i)/\tau_n^*(V_i) \\ s_i' &= \alpha_s(1 - s_i)s_\infty(V_j) - s/\tau_s, \end{aligned} \tag{5}$$

where the prime symbol denotes differentiation with respect to T and where h_i is incorporated implicitly as a parameter. We can also rescale time, introducing $\tau = \epsilon T$ as a variable that changes slowly relative to T , recast system (1–4) in terms of differentiation with respect to τ , and divide through by ϵ to obtain the slow or outer subsystem

$$\begin{aligned} 0 &= F(V_i, h_i, n_i) \\ \dot{h}_i &= (h_\infty(V_i) - h_i)/\tau_h^*(V_i) \\ 0 &= (n_\infty(V_i) - n_i)/\tau_n^*(V_i) \\ 0 &= \alpha_s(1 - s_i)s_\infty(V_j) - s/\tau_s. \end{aligned} \tag{6}$$

In the remainder of this section, since we consider single-cell dynamics, we drop the subscript i on our dependent variables.

To understand the dynamics associated with these systems, a bifurcation analysis of the fast subsystem (5) can be performed, using h as a bifurcation parameter (Rinzel 1985). The left panel of Fig. 1 shows an example of a resulting bifurcation diagram, which is very similar to that shown in Best et al. (2005), augmented with the h -nullcline, for a fixed parameter set in the self-coupled case. The intersection of the h -nullcline with the critical manifold S is a critical

point, p_0 , of the full system (1–4). An unstable family of periodic orbits emerges from S in a subcritical Andronov–Hopf (AH) bifurcation, say at $h = h_{AH}$. This family meets another stable family of periodic orbits, \mathcal{P} , in a saddle-node of periodic orbits (SNPO) bifurcation at $h > h_{AH}$. In the diagrams in Fig. 1, the family \mathcal{P} ends in an orbit homoclinic to a point on the middle branch of S , at $h_{HC} < h_{AH}$. For some other parameter values, the corresponding family, \mathcal{P} , ends in a second SNPO bifurcation, where it meets a third family of periodic orbits. This third family is unstable and terminates in an orbit homoclinic to a point on S (see Best et al. 2005).

The attractor in the configuration shown in the left panel of Fig. 1 is the critical point p_0 on the lower branch of S , where the h -nullcline meets S . The dynamics associated with the approach to this attractor is called *quiescence*, since no spikes are generated (possibly after an initial transient). It has been shown previously (Butera et al. 1999b; Best et al. 2005) that system (1–4) can also exhibit *square-wave bursting* or *tonic spiking* in certain parameter regimes. More precisely, increasing g_{ton} yields a transition from quiescence to bursting by changing the relative positions of S and the h -nullcline such that p_0 moves to the middle branch, and further increases in g_{ton} elicit a second transition, to tonic spiking. In tonic spiking, the downward drift in h during the high- V part of a spike is balanced by the upward drift in h in the trough of a spike. In the singular limit, the transition from bursting to tonic spiking occurs when p_0 moves in a direction of decreasing h through $h = h_{HC}$, when h_{HC} exists, or when h decreases through an analogous point when h_{HC} does not exist. The right panel of Fig. 1 shows a configuration with p_0 at an h -value before h_{HC} , predicted to give tonic spiking for ϵ sufficiently small. Varying g_{syn} has different effects on the bifurcation diagram and resulting dynamics, with increases in g_{syn} from 0 initially

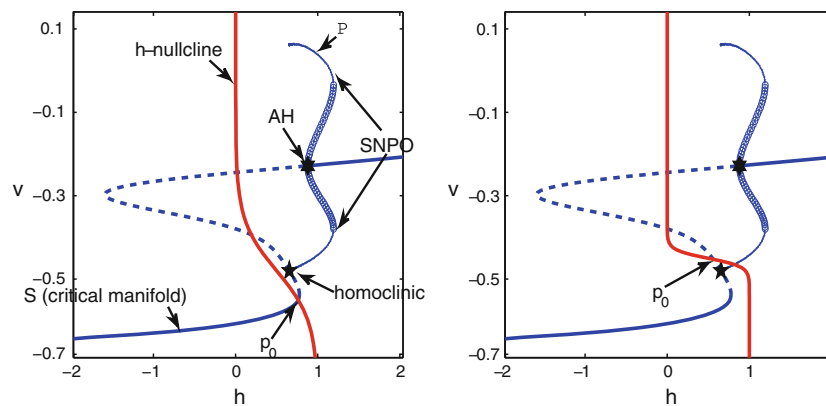


Fig. 1 Bifurcation diagrams for the fast subsystem (5), with respect to parameter h , with h -nullcline superimposed. *Left*: diagram for $g_{syn} = 0$ and $g_{ton} = 0.2$, similar to that shown by Best et al. (2005). Here p_0 is a stable critical point for the full system (1–4), corresponding to the quiescent state. The *star* indicates a homoclinic point at

$h = h_{HC} < h_{AH}$, where h_{AH} is the h -value at which an Andronov–Hopf (AH) bifurcation occurs. *Right*: a configuration, with p_0 now occurring at $h < h_{HC}$ and unstable, predicted to give tonic spiking for small ϵ

expanding the bursting region and later contracting it again (see Butera et al. 1999b; Best et al. 2005). Interestingly, for an appropriate interval of g_{ton} that yields tonic spiking with $g_{\text{syn}} = 0$, increasing g_{syn} can switch the system back to bursting, showing that dynamic synapses could play a role in promoting bursting, a functionally relevant activity pattern of the preBötC.

2.2 Two-cell dynamics

Best et al. (2005) noted that when a pair of coupled cells is considered, the range in $(g_{\text{ton}}, g_{\text{syn}})$ over which bursting occurs is enhanced even further than in the self-coupled case, matching the simulations of Butera et al. (1999b). A system of two coupled cells includes two slow variables, h_1, h_2 , and hence the fast–slow decomposition approach becomes more complicated. When both cells are in the silent phase, their dynamics are well approximated by solutions to the slow subsystem (6). Best et al. computed the net drift in the h_i when both cells are in the active phase by using the method of averaging. That is, at any (h_1, h_2) for which the two-cell fast subsystem exhibits a stable periodic oscillation $\mathcal{L}(h_1, h_2)$ with period $\Lambda(h_1, h_2)$,

$$\mathcal{L}(h_1, h_2) = \left\{ (V_1(T), n_1(T), s_1(T), V_2(T), n_2(T), s_2(T)) \in \mathbb{R}^6, T \in [0, \Lambda(h_1, h_2)]) \right\},$$

the dynamics of the slow variables with respect to the slow time $\tau = \epsilon T$ is given, up to $O(\epsilon)$, by the averaged slow equations

$$\dot{h}_i = \frac{1}{\Lambda(h_1, h_2)} \int_0^{\Lambda(h_1, h_2)} g_i(V_i(\xi)) d\xi \quad i = 1, 2. \tag{7}$$

In Eq. 7, $g_i(V_i) \equiv (h_\infty(V_i) - h_i)/\tau_h^*(V_i)$ and critical points where $\dot{h}_1 = \dot{h}_2 = 0$ correspond to periodic (tonic spiking) solutions of the full system (1–4) for the two cells (Pontryagin and Rodygin 1960). Based on Eq. 7, h_i -nullclines, \mathcal{N}_i , were computed numerically, and four dynamic regimes were identified: symmetric bursting (SB), asymmetric bursting, asymmetric spiking, and symmetric spiking (Best et al. 2005). Figure 2 illustrates the regions in $(\bar{g}_{\text{ton}}, \bar{g}_{\text{syn}})$ parameter space on which these regimes were found to arise, while Fig. 3 shows phase portraits for system (7) representative of each regime.

Here we briefly describe the regimes found and analyzed by Best et al. (2005). Let \mathcal{O} denote the region in the $h_1 - h_2$ plane, such that for each $(h_1, h_2) \in \mathcal{O}$ the fast subsystem (5) has a stable periodic orbit $\mathcal{L}(h_1, h_2)$. Numerically, the boundary $\text{bd}(\mathcal{O})$ of \mathcal{O} inside the relevant square $[0, 1] \times [0, 1]$ is observed to consist of two curves, with reflection symmetry across the line $\{h_1 = h_2\}$. In each of Fig. 3a–c, the region

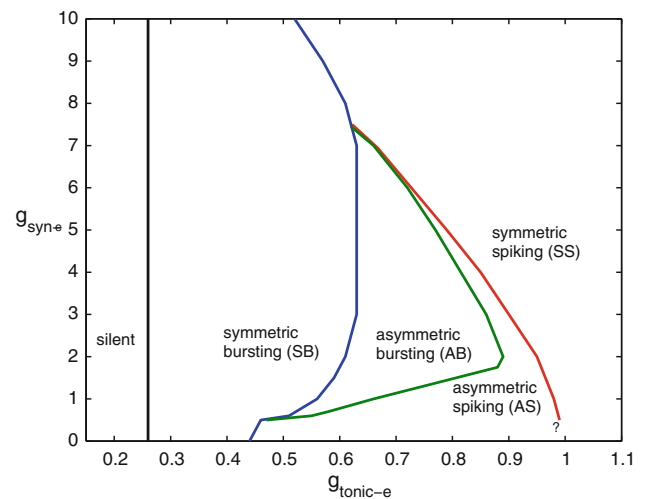


Fig. 2 Boundaries for different regimes of activity on the parameter space $(\bar{g}_{\text{ton}}, \bar{g}_{\text{syn}})$. Figure reproduced from Best et al. (2005) (Copyright(c)2005 Society for Industrial and Applied Mathematics. Reprinted with permission. All rights reserved)

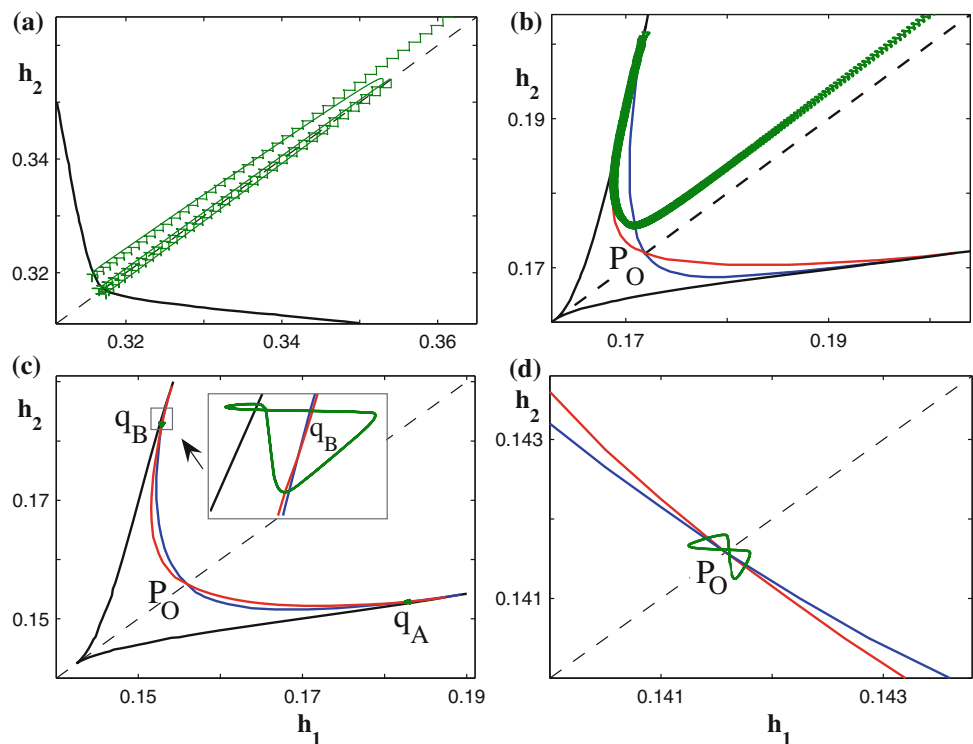
\mathcal{O} is above and to the right of these two curves, which are solid and black. Consider $(\bar{g}_{\text{ton}}, \bar{g}_{\text{syn}})$ fixed such that no stable critical point exists for (h_1, h_2) outside of \mathcal{O} .

In the SB regime (Fig. 3a), $\dot{h}_1 < 0$ and $\dot{h}_2 < 0$ for all $(h_1, h_2) \in \mathcal{O}$. Hence, trajectories starting in \mathcal{O} leave through $\text{bd}(\mathcal{O})$. Outside of \mathcal{O} , $s_i \downarrow 0$ on the fast timescale, such that the two cells decouple, and each cell evolves along the lower branch of S (Fig. 1) until one cell reaches the lower knee of S and jumps back to \mathcal{O} , pulling the other cell with it due to the resumption of synaptic excitation. This cycle repeats, yielding bursting dynamics consisting of alternating phases of fast system quiescence and phases of fast subsystem oscillations. In simulations, trajectories approach $\{h_1 = h_2\}$ as time advances.

In asymmetric bursting (Fig. 3b), unlike the previous case, there are curves in \mathcal{O} where \dot{h}_1 or \dot{h}_2 changes sign, which form the nullclines \mathcal{N}_i of (7) in \mathcal{O} . By symmetry, they intersect at a point, call it $P_{\mathcal{O}}$, in $\{h_1 = h_2\}$. With (h_1, h_2) fixed at $P_{\mathcal{O}}$, the fast subsystem exhibits a stable oscillation, and there is no net drift of (h_1, h_2) over each period, such that this represents a stationary state of the full system (in the singular limit, which perturbs to a dynamically equivalent nearby state for ϵ sufficiently small). However, $P_{\mathcal{O}}$ can be shown to be a saddle point for system (7). Trajectories near the stable manifold of $P_{\mathcal{O}}$, namely the line $\{h_1 = h_2\}$, that approach a neighborhood of $P_{\mathcal{O}}$ cross the h_2 -nullcline and are kicked out along the unstable manifold of $P_{\mathcal{O}}$ until they reach $\text{bd}(\mathcal{O})$ and exit \mathcal{O} . As in SB, this exit decouples the cells, leading to a silent phase followed by reinjection into \mathcal{O} . Bursting dynamics, with a relatively long active phase due to passage near the saddle $P_{\mathcal{O}}$, results.

In the asymmetric spiking regime (Fig. 3c), there are two additional intersection points of $\mathcal{N}_1, \mathcal{N}_2$, located off of

Fig. 3 The four dynamic regimes discussed in the text for $\bar{g}_{\text{syn}} = 3$ and $\bar{g}_{\text{ton}} = 0.56$, $\bar{g}_{\text{ton}} = 0.83$, $\bar{g}_{\text{ton}} = 0.87$ and $\bar{g}_{\text{ton}} = 0.91$, respectively. Note the difference in scales in different panels; in particular, *d* shows a zoomed view of a small neighborhood of P_O . Figure reproduced from Best et al. (2005) (Copyright (c)2005 Society for Industrial and Applied Mathematics. Reprinted with permission. All rights reserved)



$\{h_1 = h_2\}$ but equivalent under reflection across $\{h_1 = h_2\}$, and these are stable critical points of system (7). Corresponding to each of these, the full system exhibits a stable state in which the fast variables undergo large amplitude oscillations while the slow variables periodically drift around the critical point, representing tonic spiking solutions with $h_2 > h_1$ and with $h_1 > h_2$, respectively.

Finally, symmetric spiking (Fig. 3d) results after a pitchfork bifurcation for system (7) occurs. This bifurcation destroys the two previously stable critical points and stabilizes the one on $\{h_1 = h_2\}$, yielding tonic spiking in which $h_1 \approx h_2$.

3 Self-coupled cell: one-dimensional map

In this section, we derive a one-dimensional map representing the dynamics of a self-coupled cell given by (1–4), directly following Medvedev (2005). We subsequently analyze its properties and consider the dynamics of the map, with particular attention to transitions between bursting and spiking.

3.1 Derivation of the one-dimensional map

Consider the slow Eq. 2 for a fixed g_{syn} . Define a new time variable $t(T)$ (distinct from t in the original Butera model in Appendix A) such that $\frac{d}{dt} = \tau_h^*(V) \frac{d}{dT}$. Then, $t(T) = \int_0^T [1/\tau_h^*(V(\xi))] d\xi$ and Eq. 2 simplifies to

$$\frac{dh}{dt} = \epsilon(h_\infty(V) - h). \tag{8}$$

As noted in Sect. 2.1, the fast subsystem has a family of stable periodic orbits, \mathcal{P} , for each h within a range, which can be denoted as (h_L, h_R) , where the SNPO bifurcation that gives birth to \mathcal{P} (Fig. 1) occurs at $h = h_R$. For any $\eta \in (h_L, h_R)$, let \mathcal{P}_η denote the corresponding member of \mathcal{P} and let Σ_η denote a local section transversal to \mathcal{P}_η in (V, n, s) space. Without loss of generality, we can choose Σ_η as a surface of constant n at the minimum of V along \mathcal{P} , since $\dot{n} \neq 0$ there, assuming the minimum occurs at $V < \theta_{\text{syn}}$, such that $\dot{s} < 0$. Indeed, if $\dot{n} = \dot{V} = 0$ and $\dot{s} < 0$ at a point, then $d^2V/dt^2 = -(\partial I_{\text{syn}}/\partial s)\dot{s} < 0$, contradicting the fact that the point is a minimum of V . In fact, $\dot{n} < 0$ must hold there, since $n_\infty(V)$ is monotone increasing. Since the curve of minima in V along \mathcal{P} is differentiable by the implicit function theorem, $\Sigma := \cup_{\eta \in (h_L, h_R)} \Sigma_\eta$ is a local transversal to \mathcal{P} .

For any $(V(0), n(0), s(0)) \in \Sigma_\eta$ for $\eta \in (h_L, h_R)$, define

$$t_s(\eta) = \min\{t > 0 : (V(t), n(t), s(t)) \in \Sigma \text{ and } \dot{n} < 0\}.$$

Define the first return map by

$$P(\eta) = h(t_s(\eta)). \tag{9}$$

Adding ϵh on both sides of Eq. 8, multiplying it by its integrating factor $e^{\epsilon t}$, and integrating from 0 to $t_s(\eta)$ yields

$$e^{\epsilon t_s(\eta)} h(t_s(\eta)) - h(0) = \epsilon \int_0^{t_s(\eta)} h_\infty(V) e^{\epsilon t} dt.$$

Substitution of (9) then gives an equation for the first return map for the self-coupled case,

$$P(\eta) = e^{-\epsilon t_s(\eta)} \eta + \epsilon \int_0^{t_s(\eta)} h_\infty(V) e^{\epsilon(t-t_s(\eta))} dt, \quad h_L < \eta < h_R. \tag{10}$$

To complete the definition of the map, let h_L denote the h value such that the family \mathcal{P} ends as $h \rightarrow h_L^+$ (i.e., as h approaches h_L from above), either in a homoclinic orbit (such that $h_L = h_{HC}$) or in a second saddle node bifurcation of periodic orbits. We note that for $h < h_L$, the unique stable state of the fast subsystem is the critical point $(V^*(h), n^*(h), s^*(h))$ on the lower branch of the critical manifold \mathcal{S} . Trajectories that approach a neighborhood of this branch evolve under the slow flow

$$\dot{h} = \epsilon(h_\infty(V^*(h)) - h) > 0$$

until $h = h_{SN}$ is reached and the active phase is resumed. Hence, for $\eta \leq h_L$, we set $P(\eta) = h_{SN}$. This assignment completes the definition of the map $P(\eta)$ for $\eta \in (h_l, h_R)$, for any choice of $h_l < h_L$.

Now, define a function (Medvedev 2005),

$$F(\eta) = \frac{\int_0^{t_s(\eta)} h_\infty(V(t)) e^{\epsilon(t-t_s(\eta))} dt}{\int_0^{t_s(\eta)} e^{\epsilon(t-t_s(\eta))} dt}. \tag{11}$$

Some algebraic manipulations allow us to write Eq. 10 as

$$P(\eta) = e^{-\epsilon t_s(\eta)} (\eta - F(\eta)) + F(\eta), \tag{12}$$

with $P(\eta) = \eta$ if and only if $F(\eta) = \eta$. Hence, it becomes helpful to analyze $F(\eta)$, to gain insight about the form of $P(\eta)$.

3.2 Properties of the one-dimensional map

First, assume that the curve of periodic orbits \mathcal{P} ends in a homoclinic orbit \mathcal{H} at $h = h_{HC}$. The function $F(\eta)$ can be seen to have several properties for $\eta \in (h_{HC}, h_R)$:

1. $F(\eta)$ is a smooth function with $0 < F(\eta) < 1$,
2. $F(\eta)$ is a monotone decreasing function,
3. $F(\eta) \rightarrow h_\infty(V_{HC})$ as $\eta \rightarrow h_{HC}^+$,
4. for ϵ sufficiently small, $\frac{dF}{d\eta} \rightarrow -\infty$ as $\eta \rightarrow h_{HC}^+$.

All of these properties can be inferred from numerical simulations (see Fig. 4). Properties 1, 3, and 4 are also supported by analytical calculations, as detailed in Appendix B.

Alternatively, if \mathcal{P} ends in a saddle node of periodic orbits as h decreases, the periods along the family remain finite. In this case, of the properties of $F(\eta)$ mentioned above, only the first two still hold, as can be observed numerically.

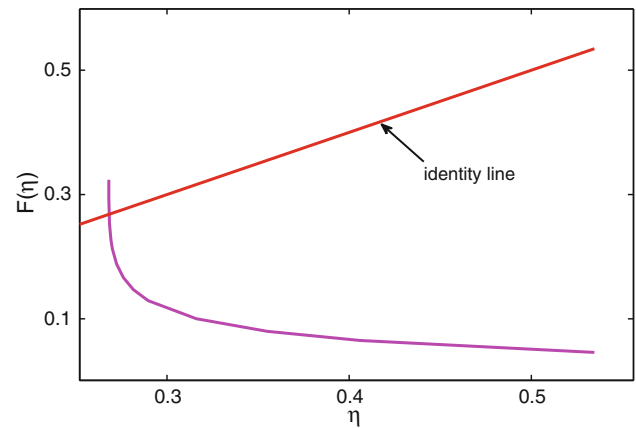


Fig. 4 $F(\eta)$ for $g_{ton} = 0.025$ and $g_{syn} = 0.1$ (equivalent to $\bar{g}_{ton} = 0.70$ and $\bar{g}_{syn} = 2.8$ in the original system)

The enumerated properties of $F(\eta)$ yield corresponding properties of $P(\eta)$. Specifically, if the homoclinic termination occurs, then

1. there exists $\eta_0 \in (h_{HC}, h_{SN})$ such that $0 < dP/d\eta < 1$ and $P(\eta) < \eta$ both hold for $\eta \in [\eta_0, h_{SN}]$ and ϵ sufficiently small,
2. $P(\eta) \rightarrow h_\infty(V_{HC})$ as $\eta \rightarrow h_{HC}^+$, since, in Eq. 12, $e^{-\epsilon t_s(\eta)} \rightarrow 0$ and $F(\eta) \rightarrow h_\infty(V_{HC})$ as $\eta \rightarrow h_{HC}^+$, and
3. $dP/d\eta \rightarrow -\infty$ as $\eta \rightarrow h_{HC}^+$.

The first property can be seen, as in Medvedev (2005), by fixing $\eta \in (h_{HC}, h_{SN})$ and using continuous dependence on ϵ to write

$$t(\eta) = t_0(\eta) + O(\epsilon), \\ (V(t), n(t), s(t)) = (V_0(t), n_0(t), s_0(t)) + O(\epsilon), \\ 0 \leq t \leq t(\eta),$$

where $(V_0(t), n_0(t), s_0(t))$, $t > 0$ is the periodic solution of the fast subsystem with $h = \eta$, with period $t_0(\eta)$. Substitution into (12) and Taylor expansion yields

$$P(\eta) = (1 - \epsilon t_0(\eta)) \eta + \epsilon t_0(\eta) F(\eta) + O(\epsilon^2).$$

Hence, we can bound $t_0(\eta)$ by choosing η above h_{HC} and then fix ϵ sufficiently small such that the desired property holds.

The third property follows from differentiating Eq. 12 with respect to η , which gives

$$\frac{dP}{d\eta} = e^{-\epsilon t_s(\eta)} + \frac{dF}{d\eta} (1 - e^{-\epsilon t_s(\eta)}) + e^{-\epsilon t_s(\eta)} \epsilon \frac{dt_s(\eta)}{d\eta} (F(\eta) - \eta). \tag{13}$$

As $\eta \rightarrow h_{HC}^+$, $t_s(\eta) \rightarrow \infty$, $dF/d\eta \rightarrow -\infty$, and $e^{-\epsilon t_s(\eta)} dt_s(\eta)/d\eta = -e^{-\epsilon t_s(\eta)} (\sigma/(\eta - h_{HC})) \rightarrow 0$, while $F(\eta)$ remains bounded, yielding the desired result.

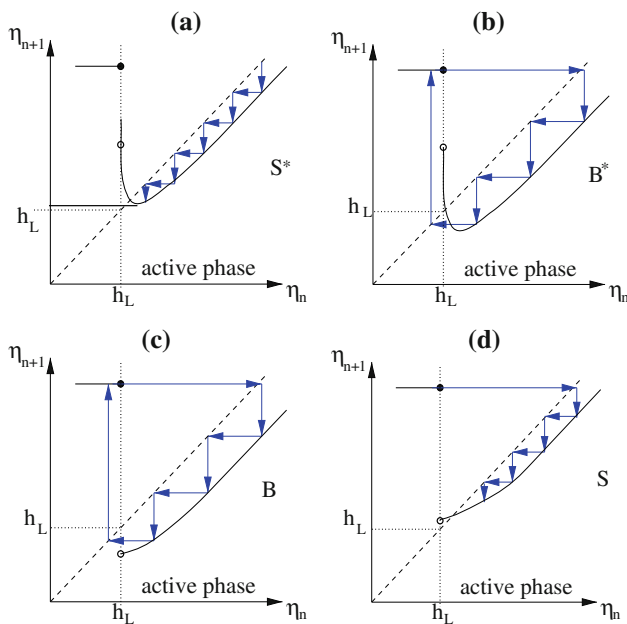


Fig. 5 The four possible forms of the map P and associated dynamic regimes that can be achieved by varying $g_{\text{syn}}, g_{\text{ton}}$. Here, S corresponds to spiking and B to bursting. Superscript $*$ denotes that there exists an $\eta^* > h_L$ such that $P'(\eta^*) = 0$. In the S^* regime, note that $\min_{\eta > h_L} P(\eta) > h_L$, such that trajectories cannot leave the active phase

From continuity of the map, the above properties yield a fixed point on $(h_{\text{HC}}, h_{\text{SN}})$ for ϵ sufficiently small, assuming that \mathcal{P} ends in a homoclinic orbit. A more detailed analysis of the transition between the linear region and the homoclinic orbit is given elsewhere for an analogous system (Medvedev 2005). If \mathcal{P} does not end in a homoclinic orbit, then the periods along \mathcal{P} may stay relatively small and $dP/d\eta$ may fail to become negative as $\eta \rightarrow h_{\text{HC}}^+$, and correspondingly a fixed point of the map P may fail to exist.

3.3 Dynamics of the one-dimensional map

The properties stated in the previous subsection provide constraints on the form P can take. For any fixed parameter values, we can assign P to one of four classes, such that maps within the same class give rise to qualitatively similar dynamics. These four classes are illustrated schematically in Fig. 5; note that we assume that P has at most one local minimum point based on numerical observations. The four classes are distinguished by two properties: (i) whether the minimum value of $P(\eta)$ lies above or below h_L , the h -value at which \mathcal{P} terminates, and (ii) whether or not there exists $\eta^* > h_L$ such that $P'(\eta^*) = 0$.

Importantly, we use property (i) to classify the dynamics associated with a parameter set as bursting or spiking. That is, if $P(\eta) < h_L$, then the trajectory leaves the active phase and $P^2(\eta) = h_{\text{SN}}$, corresponding to reset after passage through the silent phase, results. Alternatively, if $P(\eta) > h_L$ for all η ,

then the solution must remain in the active phase for all time. Thus, a necessary condition for bursting is that the minimum value of $P(\eta)$ lies below h_L . Technically, this condition is not sufficient to ensure that bursting is observed, since trajectories may not be forced close to η values near the minimum of P , yet numerics suggest that such exceptions occur only within small transitional parameter ranges, if at all.

We noted in Sect. 3.2 that when \mathcal{P} ends in a homoclinic orbit, there exists $\eta^* > h_L$, as stated in property (ii). If \mathcal{P} ends in a SNPO, then such η^* will exist if and only if the period $T(\eta)$ grows sufficiently large as $\eta \rightarrow h_L^+$. Figure 5 shows an example from each class, with the corresponding form of dynamics indicated by a cobwebbing trajectory and a text label.

When \mathcal{P} terminates in a homoclinic orbit, only the regimes shown in Fig. 5a,b are possible. When the termination is in a SNPO, however, all four regimes could occur if $T(\eta)$ were sufficiently large near η_L ; otherwise, only those in Fig. 5c,d are possible. From continuity with respect to parameters, it is clear that there are two pathways from spiking with a homoclinic termination, as seen with g_{syn} small and g_{ton} above some threshold, to bursting: either η^* can pass below η_L , corresponding to a switch from Fig. 5a to 5b, or the local minimum of P can be lost, after which $\lim_{\eta \rightarrow h_L^+} P(\eta)$ can pass from above h_L^+ to below it. We can describe each pathway in more precise mathematical terms, such as in the following proposition.

Proposition 1 *Suppose that for some small $g_{\text{syn}} \geq 0$ the cell is spiking and \mathcal{P} terminates in a homoclinic orbit at $h = h_{\text{HC}}$. The onset of bursting occurs, as g_{syn} increases through g_{syn}^* , if the following conditions hold: For each $g_{\text{syn}} \in (g_{\text{syn}}^* - \xi, g_{\text{syn}}^* + \xi)$ and $0 < \xi \ll 1$, there exists $\eta^*(g_{\text{syn}}) \in (h_{\text{HC}}, h_R)$ such that*

1. $\frac{dP}{d\eta}(\eta^*(g_{\text{syn}}), g_{\text{syn}}) = 0$,
2. $P(\eta^*(g_{\text{syn}})) = h_{\text{HC}}$, and
3. $\frac{dP}{dg_{\text{syn}}}(\eta^*(g_{\text{syn}}), g_{\text{syn}}) < 0$.

Other pathways between dynamic regimes are similar, and these pathways help determine the types of dynamics occurring between pure tonic spiking and bursting, as analyzed elsewhere (Terman 1991; Medvedev 2005). On the other hand, a direct transition between spiking with a critical point of P and bursting with no critical point of P (Fig. 5a,c), or between bursting with a critical point of P and spiking with no critical point of P (Fig. 5b,d), generically will not occur through variation of a single parameter, as they would require simultaneous changes in both properties (i) and (ii).

We conclude this section with some numerical results, obtained using a combination of XPPAUT (Ermentrout 2002) and MATLAB (The MathWorks, Inc. 2008). Figure 6 shows

Fig. 6 $P(\eta)$ for $g_{\text{ton}} = 0.025$ (equivalent to $\bar{g}_{\text{ton}} = 0.70$ in Butera et al. 1999a,b), for a single self-coupled cell, with $g_{\text{syn}} = 0.10$ (top, left) and $g_{\text{syn}} = 0.11$ (top, right), near the transition from spiking to bursting, and with $g_{\text{syn}} = 0.47$ (bottom, left) and $g_{\text{syn}} = 0.48$ (bottom, right), near the transition from bursting back to spiking. In each panel, the horizontal dashed line represents the level of η where \mathcal{P} terminates ($\eta = h_L$ in the text) and the termination mechanism is indicated ($P(\eta_*) = h_{\text{HC}}$ for homoclinic, $P(\eta_*) = h_{\text{SN}}^p$ for SNPO). The part of \mathcal{P} corresponding to reset in the silent phase ($P(\eta) = h_{\text{SN}}$) has been omitted from the bottom two panels

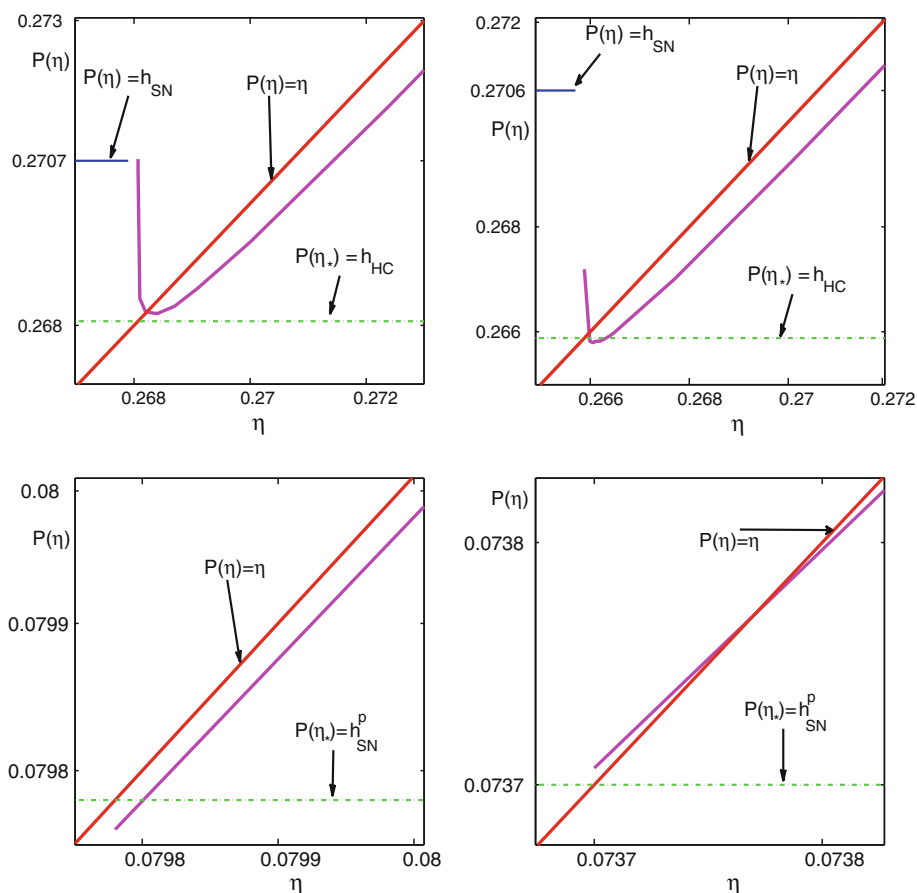


Table 1 Values of h_L computed with AUTO (Ermentrout 2002) and the lowest value of $P(\eta)$

g_{syn}	h_L	$P(\eta_{\text{min}})$
0.10	0.2680692	0.26819
0.11	0.26588065	0.26579
0.47	0.07978	0.07976
0.48	0.07368	0.073686

an example of each regime from Fig. 5, generated by varying g_{syn} with fixed g_{ton} . Table 1 shows the values h_L and the minimum value of the map for the cases in Fig. 6, confirming that all four regimes really are represented. Results of cobwebbing, implemented numerically for two of the regimes, are shown in Fig. 7. In Fig. 8, the voltage time course generated by the full system (1–4) is displayed, illustrating a full agreement with the predictions of the map analysis. Interestingly, the two bursting solutions (top right and bottom left) exhibit very different burst duration and intraburst frequency. For the upper right case, \mathcal{P} ends in an orbit of long (possibly infinite) period, manifested in Figs. 6 and 5b by the sharp slope of \mathcal{P} near its point of discontinuity. Hence, spikes slow near the end of the active phase, yielding the slowed intraburst frequency. Similarly, spike frequencies within tonic spiking solutions depend on the proximity of the fixed point

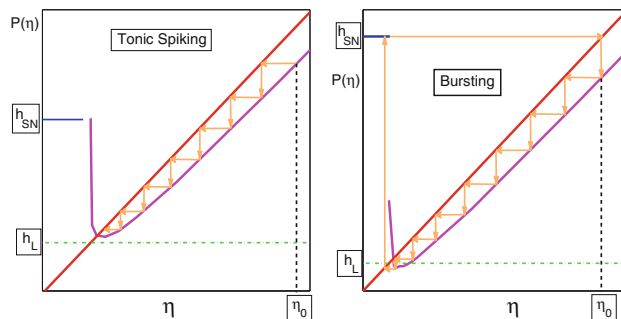
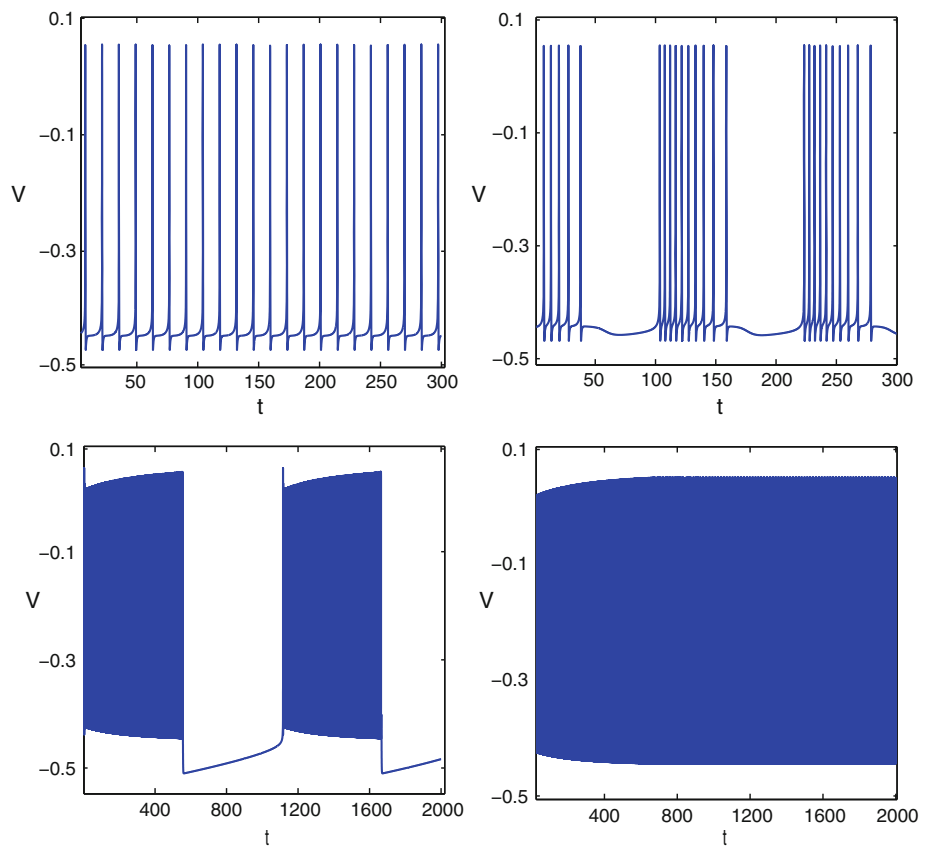


Fig. 7 Cobwebbing of the maps on Fig. 6 for $g_{\text{ton}} = 0.025$ (equivalent to $\bar{g}_{\text{ton}} = 0.70$ in Butera et al. 1999a,b), for a single self-coupled cell and $g_{\text{syn}} = 0.1$ and $g_{\text{syn}} = 0.11$, implemented numerically

to h_L and on whether h_L corresponds to a homoclinic point or SNPO.

In summary, we have used a previously introduced approach (Medvedev 2005) to derive a one-dimensional map from a four-dimensional system of ordinary differential equations, representing a single, self-coupled preBötC cell. Certain properties of this map determine the possible pathways for transitions between bursting and spiking as parameters are varied. Numerical simulations show that all of the identified dynamic regimes can be realized by varying g_{syn} . In the next section, we derive a two-dimensional map for a pair of

Fig. 8 Simulated voltage traces for the full system (1–4) for the four parameter sets used to generate Fig. 6, showing that the transitions from spiking to bursting and bursting to spiking occur as the map predicts



coupled cells, as a tool for analytically characterizing transitions between different forms of dynamics in that system.

4 Two coupled cells: two-dimensional map

Consider Eqs. 1–4 for $i, j = 1, 2$ and $j = 3 - i$, describing the dynamics of a coupled pair of cells. As discussed in Sect. 2.2, numerical simulation of averaged slow equations can be used to study activity patterns, and transitions between activity patterns, generated by this system. To get an analytical handle on the system’s dynamics, we generalize the approach from the previous section to derive and study a two-dimensional map.

As in the one-dimensional case in Sect. 3.1, we assume that the fast subsystem has a family of periodic orbits \mathcal{P} , now a two-parameter family parameterized by h_1 and h_2 on which both cells exhibit large-amplitude oscillations, that is stable on some connected open set $H \subset [0, 1] \times [0, 1]$ in (h_1, h_2) -parameter space. Analogously to the one-dimensional case, we can define a section Σ that is transverse to the family, which for concreteness we can choose to intersect \mathcal{P} along the curve of minima of V_1 . If we fix $(h_1, h_2) \in H$ and integrate Eqs. 1–4 from an initial condition on Σ with $\dot{n}_1(0) < 0$ and let $c = \text{sign}(\dot{n}_2(0))$, then the time of first return to Σ can be defined as

$$T_s(h_1, h_2) = \min\{T > 0 | \Phi(T) \in \Sigma \text{ and } \dot{n}_1 < 0 \text{ and } \text{sgn}(\dot{n}_2(T)) = c\}. \tag{14}$$

As in Sect. 3.1, the two-dimensional first return map $\mathbf{P}(\eta_1, \eta_2)$ can be defined on H and expressed as

$$\mathbf{P}(\eta_1, \eta_2) = \begin{bmatrix} P_1(\eta_1, \eta_2) \\ P_2(\eta_1, \eta_2) \end{bmatrix} = \begin{bmatrix} e^{-\alpha_1(T_s)}(\eta_1 - F_1) + F_1 \\ e^{-\alpha_2(T_s)}(\eta_2 - F_2) + F_2 \end{bmatrix} \tag{15}$$

where $T_s = T_s(\eta_1, \eta_2)$ from Eq. 14 and

$$\alpha_i(T_s) = \epsilon \bar{\tau}_h(V_i) T_s, \quad \bar{\tau}_h(V_i) = \frac{1}{T_s} \int_0^{T_s} (1/\tau_h^*(V_i(\xi))) d\xi,$$

$$F_i = F_i(\eta_1, \eta_2) = \frac{\int_0^{T_s} g_i(V_1(T), V_2(T)) e^{\alpha_i(T)} dT}{e^{\alpha_i(T_s)} - 1},$$

$$g_i(V_1, V_2) = \epsilon h_\infty(V_i) / \tau_h^*(V_i)$$

for $i = 1, 2$. Note that the coupling between the two cells does not appear explicitly in the expressions above but is present implicitly and will affect the behavior of each component of the map.

At least part of the boundary of the region H on which both cells oscillate corresponds to a fast subsystem bifurcation curve along which the family \mathcal{P} of stable periodic orbits

terminates. Trajectories that cross this curve may continue to exhibit large-amplitude oscillations in one component only or may feature silent phases in which neither component undergoes such oscillations. The former case may arise in certain transitional regimes and is beyond the scope of this work. In the latter case, the trajectory may approach a stable critical point in the silent phase, such that quiescence results, or the trajectory may eventually be reinjected into the active phase by crossing a saddle-node bifurcation curve. Fixing an initial condition (h_1, h_2) in the silent phase selects a unique saddle-node reinjection point, up to $O(\epsilon)$, due to the fast-slow nature of the flow of system (1–4).

4.1 Iterated map approach

Numerically, one could iterate the two-dimensional map \mathbf{P} given in (15) by fixing $(h_1, h_2) \in H$, choosing the intersection point of the corresponding periodic orbit $\mathcal{P}(h_1, h_2)$ with Σ as an initial condition for system (1–4), and integrating to the first return to Σ . It is not at all clear how to treat the two-dimensional map (15) analytically, however.

We find it useful to consider sections $P_1(\eta_1, \eta_2)$, for fixed η_2 , and $P_2(\eta_1, \eta_2)$, for fixed η_1 , of the full two-dimensional map \mathbf{P} . That is, to generate the $P_1(\eta_1, \eta_2)$ section, we fix η_2 and we vary η_1 over a range of values, say $\mathcal{E}(\eta_2) := [\eta_1^{\min}, \eta_1^{\max}]$, such that $(\eta_1, \eta_2) \in H$ for each $\eta_1 \in \mathcal{E}(\eta_2)$. For each choice of $\eta_1 \in \mathcal{E}(\eta_2)$, we choose an initial condition $\phi = (V_1, n_1, s_1, V_2, n_2, s_2)$ such that for $(h_1, h_2) = (\eta_1, \eta_2)$, ϕ is the point $\mathcal{P}(h_1, h_2) \cap \Sigma$. We integrate Eqs. 1–4 from this initial condition until a return to Σ occurs and take the value of h_1 at this return as $P_1(\eta_1, \eta_2)$. An analogous approach yields $P_2(\eta_1, \eta_2)$ for fixed η_1 . If $(\eta_1, \eta_2) \notin H$, then we assume that both cells enter the silent phase and take $P_i(\eta_1, \eta_2) = \eta_i^{SN}$, where $(\eta_1^{SN}, \eta_2^{SN})$ is the point on the saddle-node reinjection curve determined by initial condition (η_1, η_2) in the silent phase.

This use of sections allows us to visualize the iteration process simultaneously in the $(\eta_1, P_1(\eta_1, \eta_2))$ and $(\eta_2, P_2(\eta_1, \eta_2))$ planes. The key point is, since both η_1 and η_2 are updated in each iteration, we must choose a new section after each iteration to use for the subsequent iteration. An individual section that is a function of η_i is not equivalent to the one-dimensional map $P(\eta)$ generated for the self-coupled cell with $\eta = \eta_i$, because the timing of the synaptic input to the cell during the oscillation in the two-cell network may differ from the timing in the self-coupled case. Nonetheless, each section is qualitatively similar to the one-dimensional maps studied in Sect. 3, which allows us to catalog possible dynamic regimes and transitions between them for the two-cell system.

The iteration process is illustrated schematically in Fig. 9. The panels all show the P_1 component of \mathbf{P} , although the subscript is omitted; the other component would be updated

in parallel in a similar way and is not shown. The upper two panels show the section $P_1(\eta_1, \eta_2^1)$, with $\eta_2 = \eta_2^1$ fixed, as well as the first iteration step, which takes η_1^1 to $\eta_1^2 := P_1(\eta_1^1, \eta_2^1)$. The value η_2^2 is given by $P_2(\eta_1^1, \eta_2^1)$. In the left panel in the second row, a new section $P_1(\eta_1, \eta_2^2)$ is shown together with $P_1(\eta_1, \eta_2^1)$ and the second iteration step, yielding $\eta_1^3 := P_1(\eta_2^2, \eta_2^2)$. Similarly, the right panel in the second row and the panels in the third row show subsequent updates to P_1 and iterations of P_1 . Note that different sections are defined on different intervals of η_1 , since η_1^{\min} depends on η_2 , as discussed above. Interestingly, $\eta_1^5 < P_1(\eta_1^5, \eta_2^5) \equiv \eta_1^6$. Hence, the cobwebbing process reverses direction, and moves toward successively larger values of η_1 , starting in the right panel of the third row of Fig. 9. Finally, η_1^7 lies to the left of the domain of $P_1(\eta_1^6, \eta_2^6)$ (i.e., $\eta_1^7 < \eta_1^{\min}(\eta_2^6)$), such that cell 1 exits the active phase after the seventh iteration. Assuming that cell 2 exits the active phase at the same iteration, $P_1(\eta_1^7, \eta_2^7)$ is set to be the η_1 value on the saddle-node reinjection curve determined by silent phase initial condition (η_1^7, η_2^7) .

We can use linear interpolation to connect the points $(\eta_1^j, P_1(\eta_1^j, \eta_2^j))$ in the $(\eta_1, P_1(\eta_1))$ -plane. We take the curve obtained in this way as the orbit generated by what we call the *iterated map*, and we denote it by $\Gamma_1 = \Gamma_1(\eta_1)$. In an analogous way, we obtain the orbit generated by the iterated map $\Gamma_2 = \Gamma_2(\eta_2)$. For the schematic example, Γ_1 is illustrated in the bottom right panel of Fig. 9. Based on the construction of Γ_1 , a crossing of the identity line corresponds to a switch from a regime in which η_1 is decreasing on successive iterates of \mathbf{P} to a regime in which η_1 is increasing. In terms of the flow of the underlying system of differential equations, the h_1 -nullcline must therefore be crossed. Thus, a period where h_1 hardly changes occurs, and the linear interpolation between small steps in h_1 produces an appearance of smoothness. A numerical example of Γ_1 and Γ_2 is shown in Fig. 10, and the apparent smoothness in crossing the identity line is evident in the right panel.

Note that the map $\mathbf{\Gamma} := (\Gamma_1, \Gamma_2)$ does not correspond precisely to the dynamics of system (1–4), but it gives a good approximation by continuity in initial conditions for ϵ small, such that η changes by a small amount on each iteration. By construction, $\mathbf{\Gamma}$ depends quantitatively on the choice of initial condition (η_1^1, η_2^1) , but, after initial transients, the qualitative form of $\mathbf{\Gamma}$ does not depend on this choice and in fact can be used to classify possible dynamics of the two-cell system. To perform this classification, it is useful to consider possible intersections of components of $\mathbf{\Gamma}$ with the identity line. To do this, we start from the observation that the sections $P_i(\eta_1, \eta_2)$ are qualitatively similar to the one-dimensional map $P(\eta)$ analyzed in Sect. 3. A second important observation is that

$$\partial P_i / \partial \eta_j < 0 \quad (16)$$

Fig. 9 Dynamic cobwebbing to generate an iterated map. The lower right panel illustrates the iterated map that results from the cobwebbing process depicted in the other panels. Note that an iterated map generated from numerical cobwebbing would not have a local minimum at η above the branch point, as occurs in this cartoon near $\eta = \eta_6$

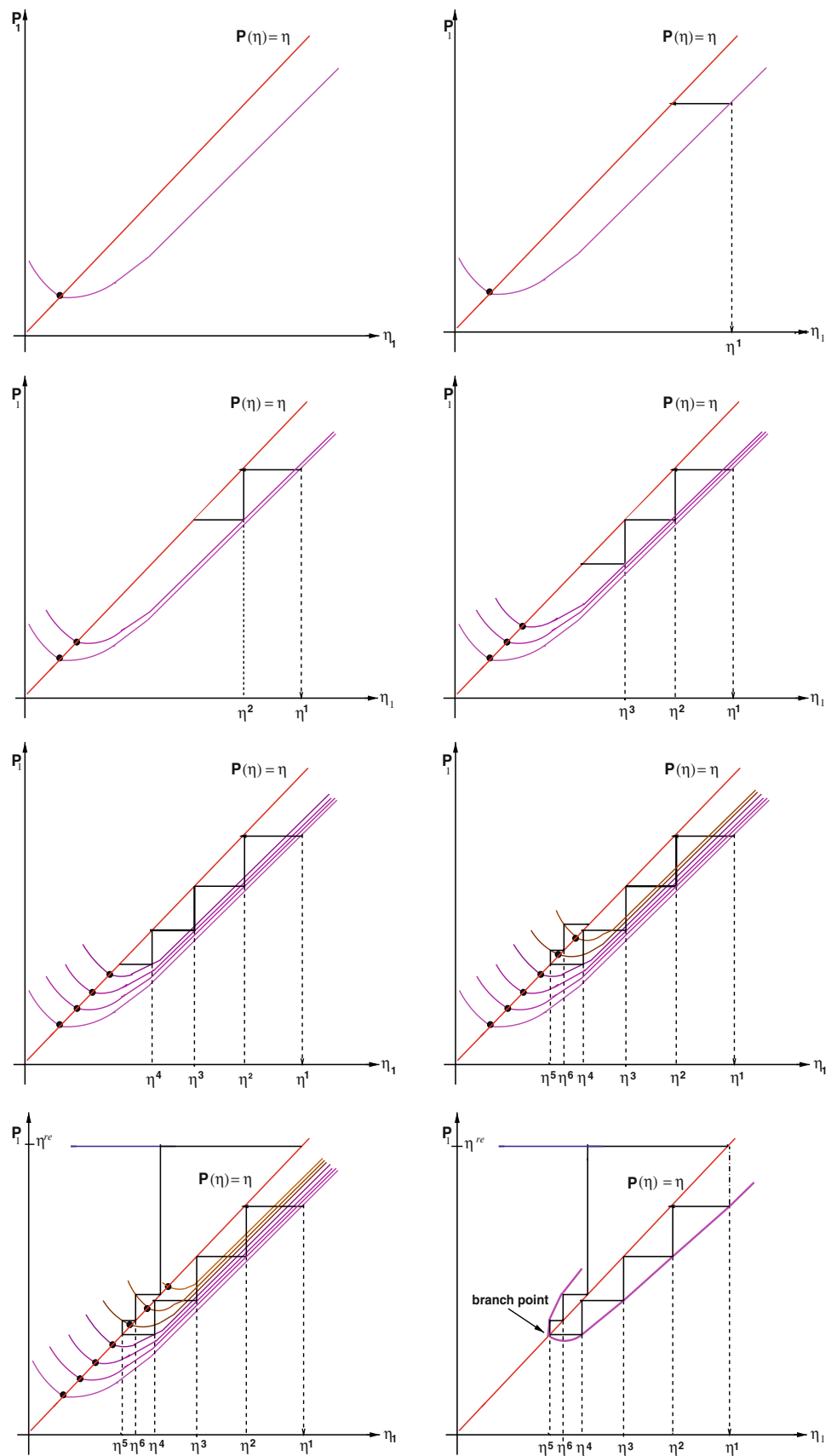
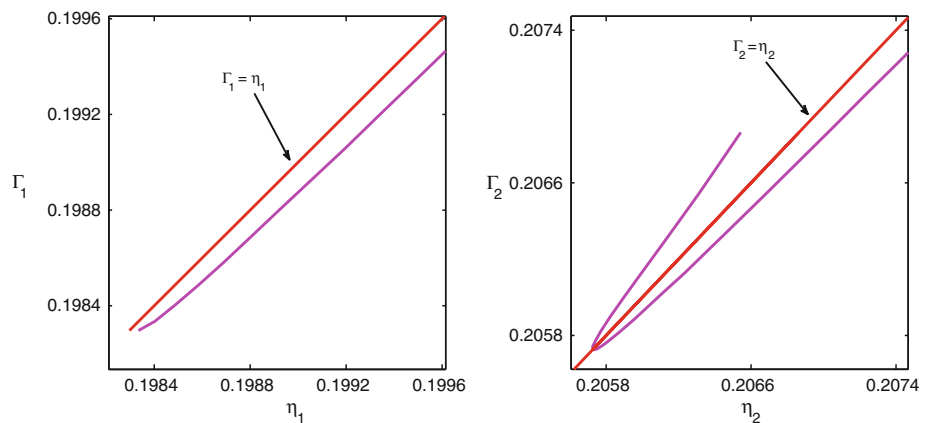


Fig. 10 Numerical computation of the iterated maps Γ_1 and Γ_2 , for $g_{\text{syn}} = 0.107143$ and $g_{\text{ton}} = 0.0275$ (corresponding to $\bar{g}_{\text{syn}} = 3$ and $\bar{g}_{\text{ton}} = 0.77$ in Best et al. 2005)



for $i \neq j \in \{1, 2\}$. This second observation is consistent with the bifurcation results derived previously (Best et al. 2005). In brief, a decrease in the initial value of h_j weakens the input from cell j to cell i during the ensuing oscillation. This weakened input causes the average voltage of cell i to be lower during this oscillation, yielding a less negative change of h_i (less inactivation) over the course of the oscillation, regardless of the initial value of h_i . Thus, $P_i(\eta_i, \eta_j)$ becomes larger for each η_i as η_j decreases.

The simplest form of Γ is one for which both components do not intersect the identity line, meaning that η_1 and η_2 both decrease throughout the active phase, as in the SB case described in Sect. 2.2 (Fig. 11, upper left panel). Alternatively, the simplest possible way that Γ_1 can intersect the identity line is if there exists η_1^* such that $\lim_{\eta_1 \rightarrow (\eta_1^*)^+} \Gamma_1(\eta_1) = \eta_1^*$ and $\Gamma_1(\eta_1)$ is an increasing function of η_1 with $\Gamma_1(\eta_1) < \eta_1$ for all $\eta_1 > \eta_1^*$, as shown in Fig. 11, upper right panel. For such a point to exist, there must be a finite or infinite sequence (η_1^j, η_2^j) such that $\eta_1^{j+1} = P_1(\eta_1^j, \eta_2^j) < \eta_1^j$ and $\eta_2^{j+1} = P_2(\eta_1^j, \eta_2^j)$ for all j , and both $\eta_1^j \rightarrow \eta_1^*$ and $P_1(\eta_1^j, \eta_2^j) \rightarrow \eta_1^*$ hold as j increases. By property (16), there must exist η_2^* such that $\eta_2^j \rightarrow \eta_2^*$ as j increases as well, to achieve the convergence of P_1 , since η_2 is constrained to a finite domain, such that $\partial P_1 / \partial \eta_2$ has a strictly negative upper bound. In summary, in this case, Γ has a fixed point, the coordinates of which both of its components approach from above, and this point is also a stable fixed point of \mathbf{P} , yielding symmetric spiking (SS) dynamics.

A third possibility is that Γ_1 has a portion of its graph below the identity line and a portion above the identity line. We shall refer to the portion below the identity line as the *lower branch* of the iterated map and denote it by **LB** and the portion of the map above the identity line as the *upper branch* and denote it by **UB**. In this case, interpolation yields a point η_1^* such that $\Gamma_1(\eta_1^*) = \eta_1^*$, connecting its **LB** and **UB**, which we call a *branch point* of Γ_1 . When Γ_1 has a branch point, Γ_2 may or may not have one, and vice versa. Moreover, for either i , the **UB** of Γ_i , when it exists, may meet the identity line in

a fixed point η_i^* , such that $P_i(\eta_1^j, \eta_2^j) \rightarrow \eta_i^*$ (Fig. 11, bottom row left), or in a second branch point, or neither (Fig. 11, bottom row right). We assume here that multiple branch points do not occur. If **UB** terminates in a fixed point for some i , then Γ_j also has a fixed point for $j \neq i$, by similar convergence arguments to those used above, although Γ_j need not have a branch point. Again, fixed points of Γ correspond to stable fixed points of \mathbf{P} , and in fact the relation is reciprocal, since convergence of \mathbf{P} yields convergence of Γ by construction.

In summary, intersection points of $\Gamma_i(\eta_i)$ with the identity line may be

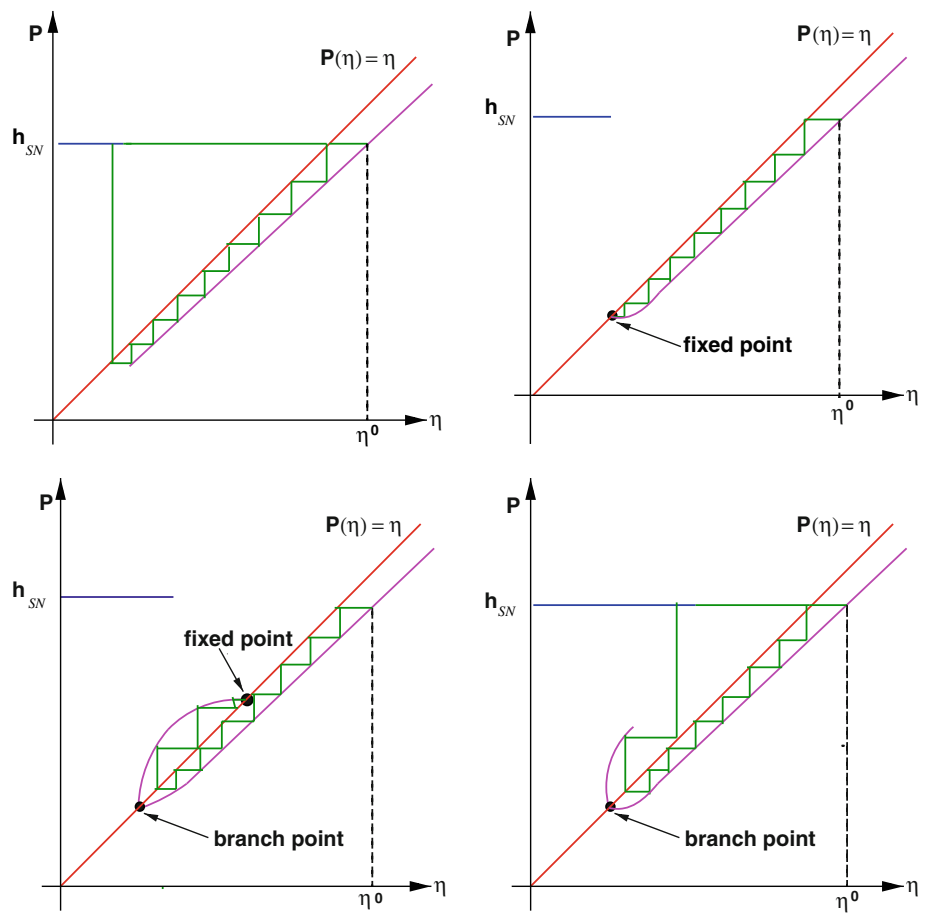
- (i) fixed points that Γ_i approaches below (above) the identity line as η_i decreases (increases), in which case they are shared by Γ_j , $j \neq i$, and correspond to stable fixed points of \mathbf{P} , or
- (ii) branch points, which do not correspond to stable fixed points of \mathbf{P} and do not imply anything about Γ_j for $j \neq i$.

Interestingly, if Γ_i has a branch point, then for iterates after the branch point is crossed, property (16) implies that $P_j(\eta_1^j, \eta_2^j)$ decreases as j increases, since η_i^j increases. Nonetheless, Γ_j may still develop a branch point, if P_j has a region of negative slope.

4.2 Dynamic regimes and transitions between them

Each qualitatively distinct form of the iterated map Γ corresponds to a specific form of dynamics of the slow averaged Eq. 7. A key observation is that η_i can change from decreasing to increasing, and a branch point of a component Γ_i can exist, if and only if the slow averaged variable h_i crosses its nullcline. That is, both of these effects occur if and only if the direction of net change in h_i over a single oscillation cycle switches from negative to positive. Moreover, as we have discussed, if Γ_i has a fixed point, then Γ_j also has a fixed point, corresponding to a stable fixed point of \mathbf{P} , which implies the existence of a stable equilibrium point of the slow averaged

Fig. 11 Four possible configurations for a component Γ_i of the iterated map $\mathbf{\Gamma}$



Eq. 7 in the oscillatory region \mathcal{O} where the fast subsystem has stable periodic orbits.

Based on these observations, we can enumerate the possible dynamic regimes that can be achieved by the possible forms of $\mathbf{\Gamma}$ that we have identified. It turns out that all possible dynamic regimes fit within the nomenclature from past work (Best et al. 2005), as reviewed in Sect. 2.2 of this paper.

1. If Γ_1, Γ_2 take the form shown in Fig. 11, upper left panel, then the slow averaged dynamics yield no nullcline crossings or equilibrium points and symmetric bursting (SB) results.
2. If one or both of the Γ_i take the form in Fig. 11, lower right panel, then at least one of the slow averaged variables crosses its nullcline, but the absence of fixed points implies that bursting still occurs. This case is asymmetric bursting (AB).
3. If one of the Γ_i takes the form in Fig. 11, lower left panel, then the other component must have a fixed point, as in the upper right and lower left panels of Fig. 11. In either case, the resulting form of dynamics is asymmetric spiking (AS), since at least one slow averaged variable crosses its nullcline and the trajectory of (7) converges to a stable equilibrium point.

4. Finally, if both of the Γ_i take the form in Fig. 11, upper right panel, then the trajectory of system (7) converges to a stable equilibrium point without a nullcline crossing, yielding symmetric spiking (SS).

We have identified two key types of points, branch points and fixed points, in the iterated map $\mathbf{\Gamma}$. Based on these ideas, we can reason out what are the possible codimension-1 transitions (i.e., transitions that can be achieved by varying a single parameter) between dynamic regimes within the two-cell network. In doing so, it also can be helpful to think about the components P_i of the original map \mathbf{P} . The following list specifies the most obvious such transitions, and after we describe these, we will address two additional subtle cases.

1. Starting from the SB regime, the codimension-1 events that can occur are the development of a fixed point and the development of a branch point. The former would establish SS dynamics, corresponding to the existence of a fixed point without a branch point, while the latter would establish AB dynamics, corresponding to the existence of a branch point without a fixed point, at least on some small parameter interval.

To understand these events in terms of the P_i , we need to distinguish how the sections of \mathbf{P} behave near the termination of the family \mathcal{P} of fast subsystem periodic orbits. Assume first that the periods of the orbits in \mathcal{P} become large near termination, such that

$$P_1(\eta_1, \eta_2) > \eta_1, \quad P_2(\eta_1, \eta_2) > \eta_2 \quad (17)$$

hold for each pair of sections P_1, P_2 of \mathbf{P} for all (η_1, η_2) sufficiently close to the termination curve.

Now, in the SB regime, there exists an iteration index i such that $\eta_1^{i+1} = P_1(\eta_1^i, \eta_2^i)$ lies outside the domain of $P_1(\eta_1, \eta_2^{i+1})$ (i.e., $\eta_1^{i+1} < \eta_1^{\min}(\eta_2^{i+1})$), and hence cell 1 enters the silent phase; further, we have assumed that cell 2 enters the silent phase on the same iteration as cell 1. By continuous variation of a single parameter, we could in theory vary \mathbf{P} such that $\eta_1^{i+1} > \eta_1^{\min}(\eta_2^{i+1})$. We have $P_1(\eta_1, \eta_2^{i+1}) > \eta_1$ for η_1 near $\eta_1^{\min}(\eta_2^{i+1})$, by (17). In particular, $P_1(\eta_1^{i+1}, \eta_2^{i+1}) > \eta_1^{i+1}$, a branch point of Γ_1 is generated, and AB dynamics results.

Alternatively, suppose that instead of (17), we have $P_1(\eta_1, \eta_2) < \eta_1$ and $P_2(\eta_1, \eta_2) < \eta_2$ for each pair of sections of \mathbf{P} . Since no branch points can form, the only alternative regime to SB is SS, and this can be achieved by variation of a parameter to generate a stable fixed point of \mathbf{P} .

2. Starting from the AB regime, a one-parameter transition to the SB regime is theoretically possible, by reversing the arguments given above. Variation of a single parameter could instead give rise to a fixed point, which would yield the AS regime, since the branch point present in AB would still be there.
3. From the AS regime, loss of the fixed point due to modulation of a single parameter would give a switch to the AB regime, corresponding to the reverse of the previous case. The SS regime can also be achieved by variation of a single parameter, if this variation causes the fixed point to collapse onto the branch point. In fact, the codimension-1 nature of the AS to SS transition may be easier to appreciate in terms of the dynamics of the slow averaged differential equations (7), where this transition corresponds to a pitchfork bifurcation within the oscillatory region \mathcal{O} (see Best et al. 2005 and Fig. 3).
4. From the SS regime, as we have already seen, transitions to AS and to SB are both possible codimension-1 events.

In fact, the above list includes exactly those transitions that were clearly distinguished in previously published simulation results on the two-cell ode model (Best et al. 2005). However, there was some ambiguity in that work relating to the two most subtle cases, namely direct transitions between SB and AS and between SS and AB.

The transition between SB and AS can in fact be achieved as a codimension-1 event, in theory. Consideration of the two-dimensional map is advantageous for understanding this transition, relative to the dynamics of the ode. In the AS regime, both components of $\mathbf{\Gamma}$ have fixed points, while at least one has a branch point. Without loss of generality, suppose that component Γ_1 has a branch point. Variation of a single parameter could cause a change in the forms of the relevant P_i yielding a switch from $\eta_1^{i+1} > \eta_1^{\min}(\eta_2^{i+1})$ to $\eta_1^{i+1} < \eta_1^{\min}(\eta_2^{i+1})$ for some i . Thus, the active phase would terminate at iteration $i + 1$, and the fixed point, which would still be present in the dynamics of (7), would not show up in the new Γ , by construction. The $(i + 1)$ st iteration could come after the crossing of the branch point, in which case AB would result, or, if the $(i + 1)$ st iteration had been the first one for which η_1 became increasing, then the branch point could disappear, yielding SB. In terms of the dynamics of (7), this form of transition would correspond to a movement of the nullclines such that trajectories that had crossed a nullcline and been attracted to a stable fixed point off of $\{h_1 = h_2\}$ in the AS regime would instead leave from \mathcal{O} without crossing a nullcline and being pushed away from $\{h_1 = h_2\}$ after the transition to the SB regime. The stable fixed point off of $\{h_1 = h_2\}$ would remain, but trajectories would enter the active phase outside of its basin of attraction under the flow of (7). In fact, this transition would yield a region in parameter space for which some trajectories in the active phase oscillatory region \mathcal{O} would leave \mathcal{O} through its boundary and others would still be attracted to the remaining stable fixed points off of $\{h_1 = h_2\}$. Such a situation is suggestive of bistability, but in fact reset from the silent phase could push trajectories toward only one of these outcomes, such that bistability would not be guaranteed.

The SS to AB transition, corresponding to replacement of a stable fixed point of $\mathbf{\Gamma}$ with a branch point of at least one of the Γ_i , is also theoretically possible through continuous variation of a single parameter. To understand why, it is in this case most convenient to think in terms of the dynamics of the differential equation system (7). Recall that from the SB regime, a transition to the SS regime will occur if variation of a parameter causes a stable fixed point of (7) to enter the fast subsystem oscillatory region \mathcal{O} through the boundary point of \mathcal{O} on the line $\{h_1 = h_2\}$. If we turn this transition around, it suggests that an SS to SB transition will occur if parameter variation causes such a fixed point to leave \mathcal{O} through its boundary, $\text{bd}(\mathcal{O})$. The state resulting from such a modulation, however, depends on the slopes of the nullclines of (7) relative to those of the components of $\text{bd}(\mathcal{O})$ at $\{h_1 = h_2\}$. If the nullclines do not intersect \mathcal{O} after the fixed point leaves, then SB can result. If, however, a part of one nullcline lies in \mathcal{O} above $\{h_1 = h_2\}$, and by symmetry a part of the other nullclines lies in \mathcal{P} below $\{h_1 = h_2\}$ even after the fixed point leaves, then AB results. In terms of maps, the

corresponding idea is that the disappearance of a fixed point of $\mathbf{\Gamma}$ might or might not be accompanied by the appearance of a branch point of one of its components, depending on details of the slices of the two-dimensional map \mathbf{P} made relevant by variation of a parameter. In simulations, we have not previously found clear evidence of a transition from SS to AB, but much room for exploration remains.

5 Discussion

We have taken the model introduced by Butera et al. (1999a,b) for a single, self-coupled neuron in the pre-BötC, which yields quiescence, bursting, and tonic spiking as particular parameters are varied, and applied a previously developed derivation method (Medvedev (2005)) to obtain a one-dimensional map, P , representing its dynamics. The one-dimensional map tracks the evolution of the slow inactivation variable h for the persistent sodium current from one oscillation to the next while the cell is spiking, with an appropriate reinjection into the active phase if the cell falls silent. Certain properties of the map can be established analytically, and others numerically, and we have used these to delineate the possible forms of dynamics the model can produce as well as the possible codimension-one (i.e., attainable through variation of a single parameter) transitions between dynamic regimes (Figs. 5, 6). In particular, it is known that depending on parameter values, the oscillations exhibited by the model may terminate, as h is decreased, in a homoclinic bifurcation or a saddle-node bifurcation of periodic orbits for the fast subsystem consisting of the equations for the other variables in the model. Our analysis shows how the nature of this termination mechanism affects the form of the map and affects its dynamics. We have also shown numerically that all of these forms of dynamics can be obtained by varying the conductance of the synaptic current representing the neuron's self-excitation, g_{syn} (Fig. 8).

In the case of a coupled two-neuron network, as analyzed previously by numerical simulations (Butera et al. 1999b) and through fast-slow decomposition, averaging, and numerical bifurcation analysis (Best et al. 2005), a conceptually similar derivation yields a two-dimensional map, $\mathbf{P}(\eta_1, \eta_2) = (P_1(\eta_1, \eta_2), P_2(\eta_1, \eta_2))$, on the persistent sodium inactivation variables for the two neurons. Establishing the properties of two-dimensional maps and analyzing their dynamics is generally a difficult undertaking. We have noted that for each fixed η_j , the component P_i , $i \neq j$, treated as a function of η_i , is analogous to the one-dimensional map P . We have exploited this feature to generate an iterated map that can be used to approximate orbits of \mathbf{P} . This approach allows us to constrain the possible forms of dynamics that the two-neuron network can produce and the codimension-1 transitions between them, as we did in the one-cell case.

Interestingly, the possible dynamics match those seen previously (Best et al. 2005), providing an analytical confirmation that the earlier bifurcation analysis based on fast-slow decomposition and averaging covered the relevant dynamic regimes. Our analysis of transitions establishes exactly which switches between dynamic regimes are possible and hence is more comprehensive than numerical explorations alone.

We do make certain simplifying assumptions in our analysis. In particular, we assume that the two-cell network does not enter a regime in which one cell exhibits multiple oscillations while the other is silent. We also do not explore chaotic dynamics, which will arise during at least some transitions between regular dynamic regimes (Terman 1991, 1992; Medvedev 2006; Medvedev and Yoo 2008; Innocenti and Genesis 2009). Further, we neglect the possible influence of noise on system dynamics. Of course, noise is present in all neuronal systems. Because we focus on codimension-1 transitions between regimes and structurally stable forms of dynamics, our qualitative results will persist in the presence of small noise. Noise can affect times of transitions between phases in bursting dynamics (e.g., Su et al. 2004, Pedersen and Sørensen 2006/07) and, at stronger levels, can induce even more significant dynamic effects (Hitzenko and Medvedev 2009).

In past work, an increase in simulation speed, relative to differential equation models, has been cited as a motivation for the development of map-based representations of neuronal network dynamics. The derivation that we follow is theoretically attractive relative to phenomenological approaches, in that it is an analytical reduction that preserves model dynamics, but it does not yield this efficiency advantage at the network level, since it requires integration of differential equations, unlike the phenomenological approach (Rulkov 2004). Possibly other reduction methods (Channell Jr. et al. 2007) or a combination of analytical and phenomenological steps can be used to achieve both ends in future work. Another challenge is the difficulty of analyzing maps of dimension greater than one. Overcoming this difficulty, perhaps through an iterative approach as we have employed here for our two-cell network and corresponding two-dimensional map, will be necessary to broaden the applicability of maps for the mathematical analysis of neuronal networks.

Acknowledgements This work was partly supported by the U.S. National Science Foundation Award DMS 0716936 (JR).

6 Appendix A

The model for pre-BötC cells introduced by Butera et al. (1999a,b), for a network of two reciprocally cells indexed by $i = 1, 2$, takes the form

Table 2 Parameter values for the preBötC neuron model

Parameter	Value
\bar{g}_{NaP}	2.8 nS
E_{Na}	50.0 mV
$\theta_{m,P}$	-40 mV
$\sigma_{m,P}$	-6 mV
$\bar{\tau}_h$	10,000 ms
θ_h	-48 mV
σ_h	6 mV
\bar{g}_{Na}	28 nS
θ_m	-34 mV
σ_m	-5 mV
\bar{g}_{K}	11.2 nS
E_{K}	-85.0 mV
$\bar{\tau}_n$	10 ms
θ_n	-29 mV
σ_n	-4 mV
\bar{g}_L	2.8 nS
E_L	-65.0 mV
C_m	21 pF
E_{syn}	0 mV
α_s	0.2 ms ⁻¹
τ_s	5 ms
θ_s	-10.0 mV
σ_s	-5 mV

$$\begin{aligned}
 v_i' &= (-I_{\text{NaP}}(v_i, h_i) - I_{\text{Na}}(v_i, n_i) - I_{\text{K}}(v_i, n_i) \\
 &\quad - I_L(v_i) - I_{\text{ton}}(v_i) - I_{\text{syn}}(v_i)) / C_m \\
 n_i' &= (n_{\infty}(v_i) - n_i) / \tau_n(v_i) \\
 h_i' &= (h_{\infty}(v_i) - h_i) / \tau_h(v_i) \\
 s_i' &= \alpha_s(1 - s_i)s_{\infty}(v_i) - s_i / \bar{\tau}_s.
 \end{aligned} \tag{18}$$

In system (18), the intrinsic ionic currents are $I_{\text{NaP}} = \bar{g}_{\text{NaP}} m_{P,\infty}(v_i) h_i (v_i - E_{\text{Na}})$, $I_{\text{Na}} = \bar{g}_{\text{Na}} m_{\infty}^3(v_i) (1 - n_i) (v_i - E_{\text{Na}})$, $I_{\text{K}} = \bar{g}_{\text{K}} n_i^4 (v_i - E_{\text{K}})$, and $I_L = \bar{g}_L (v_i - E_L)$, while the input currents are $I_{\text{ton}} = \bar{g}_{\text{ton}} (v_i - E_{\text{syn}})$, corresponding to a constant conductance drive, and $I_{\text{syn}} = \bar{g}_{\text{syn}} s_j (v_i - E_{\text{syn}})$ for $j = 3 - i$, denoting synaptic input from the other cell. For $x \in \{m_P, m, h, n, s\}$, the function $x_{\infty}(v)$ takes the form $x_{\infty}(v) = \{1 + \exp[(v - \theta_x) / \sigma_x]\}^{-1}$, and for $x \in \{h, n\}$, the function $\tau_x(v)$ takes the form $\tau_x(v) = \bar{\tau}_x / \cos h[(v - \theta_x) / 2\sigma_x]$. Most parameter values for the model appear in the table below. The parameters \bar{g}_{ton} and \bar{g}_{syn} were varied in past work (Butera et al. 1999b) within the ranges 0 – 1.2 nS and 0 – 12 nS, respectively, to study their impact on system dynamics. Identical values were also used by Best et al. (2005) except that a parameter ϵ was specifically factored out of $\bar{\tau}_h$, as was done in Eq. 2 in this paper, and similar values were used in other works (Rubin 2006; Dunmyre and Rubin 2009).

7 Appendix B

Here we consider the properties of

$$F(\eta) = \frac{\int_0^{t_s(\eta)} h_{\infty}(V) e^{\epsilon(t-t_s(\eta))} dt}{\int_0^{t_s(\eta)} e^{\epsilon(t-t_s(\eta))} dt},$$

as stated in Sect. 3.2. The first property follows immediately from the definition of $F(\eta)$, since $h_{\infty}(V) \in (0, 1)$. For properties 3 and 4, assume that \mathcal{P} ends in a homoclinic orbit at $h = h_{\text{HC}}$.

Consider the fast subsystem dynamics for $h = h_{\text{HC}}$, which we assume exists. Choose local transversals Σ_s, Σ_u to the stable and unstable manifolds of the homoclinic point $(V_{\text{HC}}, n_{\text{HC}}, s_{\text{HC}})$ of \mathcal{H} , respectively, in a neighborhood of that point, and let t_s^0 denote the time of passage along \mathcal{H} from Σ_u to Σ_s . Write the numerator of Eq. 11 as

$$\begin{aligned}
 \int_0^{t_s(\eta)} h_{\infty}(V) e^{\epsilon(t-t_s(\eta))} dt &= \int_0^{t_s^0} h_{\infty}(V) e^{\epsilon(t-t_s(\eta))} dt \\
 &\quad + \int_{t_s^0}^{t_s(\eta)} h_{\infty}(V) e^{\epsilon(t-t_s(\eta))} dt. \tag{19}
 \end{aligned}$$

The two terms on the right hand side correspond, respectively, to the dynamics away from and close to the homoclinic point. The first integral in (19) can be written as

$$\int_0^{t_s^0} h_{\infty}(V) e^{\epsilon(t-t_s(\eta))} dt = e^{\epsilon(t_s^0-t_s(\eta))} \int_0^{t_s^0} h_{\infty}(V) e^{\epsilon(t-t_s^0)} dt \tag{20}$$

In the second integral, since V changes slowly near the homoclinic point, $h_{\infty}(V) \simeq h_{\infty}(V_{\text{HC}})$. Thus, Eq. 19 becomes

$$\begin{aligned}
 \int_0^{t_s(\eta)} h_{\infty}(V) e^{\epsilon(t-t_s(\eta))} dt &\approx e^{\epsilon(t_s^0-t_s(\eta))} \int_0^{t_s^0} h_{\infty}(V) e^{\epsilon(t-t_s^0)} dt \\
 &\quad + h_{\infty}(V_{\text{HC}}) \int_{t_s^0}^{t_s(\eta)} e^{\epsilon(t-t_s(\eta))} dt.
 \end{aligned}$$

Based on these expressions, the equation for $F(\eta)$ can be written, up to a small error that shrinks with ϵ , as

$$F(\eta) = \frac{e^{-\epsilon(t_s(\eta)-t_s^0)} A(\eta) + h_{\infty}(V_{\text{HC}})}{(1 - e^{-\epsilon t_s(\eta)})} \tag{21}$$

where $A(\eta) = \epsilon t_s^0 F_0(\eta) - h_{\infty}(V_{\text{HC}})$ and

$$F_0(\eta) = \epsilon \frac{\int_0^{t_s^0} h_{\infty}(V) e^{\epsilon(t-t_s^0)} dt}{(1 - e^{-\epsilon t_s^0})}. \tag{22}$$

From these expressions it is clear that, since $t_s(\eta) \rightarrow \infty$ as $\eta \rightarrow h_{HC}^+$, property 3 holds.

Now, differentiating (21) with respect to η yields

$$\frac{dF}{d\eta} = \epsilon \frac{e^{-\epsilon(t_s(\eta)-t_s^0)} [G(\eta) - H(\eta)]}{(1 - e^{-\epsilon t_s(\eta)})^2}$$

where

$$G(\eta) = t_s^0 \frac{dF_0}{d\eta} (1 - e^{\epsilon t_s(\eta)})$$

and

$$H(\eta) = \frac{dt_s(\eta)}{d\eta} (A(\eta) + h_\infty(V_{HC})e^{-\epsilon t_s^0}).$$

In (21), $t_s(\eta) - t_s^0$ can be written as

$$\begin{aligned} t_s(\eta) - t_s^0 &= \int_0^{T_s(\eta)} (1/\tau_h^*(V)) d\xi - \int_0^{T_s^0} (1/\tau_h^*(V)) d\xi \\ &= \int_{T_s^0}^{T_s(\eta)} (1/\tau_h^*(V)) d\xi \end{aligned} \tag{23}$$

where $T_s(\eta)$ and T_s^0 are defined similarly to $t_s(\eta)$ and t_s^0 , respectively. Again using $\tau_h(V) \approx \tau_h(V_{HC})$ near the homoclinic point yields

$$\begin{aligned} t_s(\eta) - t_s^0 &\approx (1/\tau_h^*(V_{HC})) (T_s(\eta) - T_s^0) \\ &\approx -(\log(d(\eta - \eta_{HC})))^{\mu/\tau_h^*(V_{HC})} \end{aligned} \tag{24}$$

where μ^{-1} is the positive eigenvalue of the matrix of linearization of the fast subsystem near the homoclinic point (Medvedev 2005) and $d = |f'(h_{HC})| \neq 0$, where $f(h)$ is the split function that measures the distance between the branches of the stable and unstable manifolds corresponding to the fast subsystem at h near h_{HC} (Medvedev 2005; Kuznetsov 1995).

Let $\sigma = (\epsilon\mu) / \tau_h^*(V_{HC})$, such that

$$e^{-\epsilon(t_s(\eta)-t_s^0)} \approx (d(\eta - \eta_{HC}))^\sigma. \tag{25}$$

Note that when $\epsilon \rightarrow 0$, $(d(\eta - \eta_{HC}))^\sigma \rightarrow 1$. Near the homoclinic, we also have

$$\begin{aligned} &\epsilon \int_{t_s^0}^{t_s(\eta)} h_\infty(V) e^{\epsilon(t-t_s(\eta))} dt \\ &\approx h_\infty(V_{HC})(1 - (d(\eta - \eta_{HC}))^\sigma). \end{aligned} \tag{26}$$

Thus, we can write (23) as

$$\frac{dF}{d\eta} = \frac{\epsilon[d(\eta - \eta_{HC})]^\sigma [G(\eta) - K(\eta)]}{(1 - e^{-\epsilon t_s(\eta)})^2} \tag{27}$$

where

$$K(\eta) = \frac{dt_s}{d\eta} (\epsilon t_s^0 F_0 + h_\infty(V_{HC})(e^{-\epsilon t_s^0} - 1)).$$

Consider Eq. 27. Equation 25 implies that $d^\sigma(\eta - \eta_{HC})^\sigma > 0$. Clearly, $t_s^0 > 0$ and $1 - e^{-\epsilon t_s(\eta)} > 0$, while we know $0 < F(\eta) < 1$. Differentiating $t_s(\eta)$ with respect to η , up to first order terms, yields

$$\frac{dt_s}{d\eta} = -\frac{\mu/\tau_h^*(V_{HC})}{\eta - \eta_{HC}} = -\frac{\sigma}{\epsilon(\eta - \eta_{HC})} < 0 \tag{28}$$

for $\eta > h_{HC}$. Note that $\frac{dt_s}{d\eta} \rightarrow -\infty$ as $\eta \rightarrow h_{HC}^+$. Moreover, Eq. 22 reveals that $dF_0/d\eta$ is finite, since t_s^0 is a finite constant, $h_\infty(V)$ is a smooth function, and the family \mathcal{P} of periodic orbits varies smoothly with η . Hence, the $dt_s(\eta)/d\eta$ term dominates the numerator of $F(\eta)$ in Eq. 27 as $\eta \rightarrow h_{HC}^+$.

To establish property 4, we next show that the term multiplying $\frac{dt_s(\eta)}{d\eta}$ in Eq. 27 is negative. Recall that

$$\begin{aligned} F_0(\eta) &= \frac{\epsilon \int_0^{t_s^0} h_\infty(V) e^{-\epsilon(t-t_s^0)} dt}{1 - e^{-\epsilon t_s^0}} \\ &< h_\infty(V_{HC}) \frac{\epsilon \int_0^{t_s^0} e^{-\epsilon(t-t_s^0)} dt}{1 - e^{-\epsilon t_s^0}} = h_\infty(V_{HC}) \end{aligned}$$

if $V(t) > V_{HC}$, since $h_\infty(V)$ is a non-increasing function of V . Thus,

$$\begin{aligned} &\epsilon t_s^0 F_0(\eta) + h_\infty(V_{HC})(e^{-\epsilon t_s^0} - 1) \\ &= \epsilon t_s^0 F_0(\eta) - \epsilon t_s^0 h_\infty(V_{HC}) + O(\epsilon^2) < 0 \end{aligned}$$

for ϵ sufficiently small. Since $\frac{dt_s(\eta)}{d\eta} < 0$ as well, the dominant term on the right hand side of (27) is negative, as desired. Finally,

$$(\eta - \eta_{HC})^\sigma \frac{dt_s(\eta)}{d\eta} = -\frac{\sigma(\eta - \eta_{HC})^{\sigma-1}}{\epsilon} \rightarrow -\infty \tag{29}$$

as $\eta \rightarrow \eta_{HC}^+$, which gives property 4. □

References

Altendorfer R, Koditschek D, Holmes P (2003) Stability analysis of legged locomotion by symmetry-factored return maps. *Int J Robot Res* 23:979–999

Best J, Borisyuk A, Rubin J, Terman D, Welschberger M (2005) The dynamic range of bursting in a model respiratory pacemaker network. *SIAM J Appl Dyn Syst* 4:1107–1139

Butera R, Rinzel J, Smith J (1999a) Models of respiratory rhythm generation in the pre-Bötzinger complex. I. Bursting pacemaker neurons. *J Neurophysiol* 82:382–397

Butera R, Rinzel J, Smith J (1999b) Models of respiratory rhythm generation in the pre-Bötzinger complex. II. Population of coupled pacemaker. *J Neurophysiol* 82:398–415

- Channell P Jr., Cymbalyuk G, Shilnikov A (2007) Applications of the poincaré mapping technique to analysis of neuronal dynamics. *Neurocomputing* 70:2107–2111
- Chay TR, Keizer J (1983) Minimal model for membrane oscillations in the pancreatic β -cell. *Biophys J* 42:181–190
- Ditto WL, Raueo SN, Spano ML (1990) Experimental control of chaos. *Phys Rev Lett* 65:3211–3214
- Dunmyre JR, Rubin JE (2009) Optimal intrinsic dynamics for bursting in a three-cell network. *SIAM J Dyn Syst* 9:154–187
- Ermentrout B (2002) *Simulating, Analyzing, and Animating Dynamical Systems: A Guide to XPPAUT for Researchers and Students. Software Environ. Tools 14*, SIAM, Philadelphia
- Ermentrout GB, Kopell N (1998) Fine structure of neural spiking and synchronization in the presence of conduction delays. *Proc Natl Acad Sci USA* 95(3):1259–1264
- Gomes AA, Manica E, Varriale MC (2008) Applications of chaos control techniques to a three-species food chain. *Chaos Solitons Fractals* 35:432–441
- Hitczenko P, Medvedev GS (2009) Bursting oscillations induced by small noise. *SIAM J Appl Math* 69:1359–1392
- Innocenti G, Genesio R (2009) On the dynamics of chaotic spiking-bursting transition in the Hindmarsh-Rose neuron. *Chaos* 19:023124
- Izhikevich E (2000) Neural excitability, spiking, and bursting. *Int J Bifurc Chaos* 10:1171–1266
- Kuznetsov YA (1995) *Elements of applied bifurcation theory*, vol 112 of Applied Mathematical Sciences. Springer-Verlag, Berlin
- LoFaro T, Kopell N (1999) Timing regulation in a network reduced from voltage-gated equations to a one-dimensional map. *J Math Biol* 38:479–533
- Medvedev GS (2005) Reduction of a model of an excitable cell to a one-dimensional map. *Physica D* 202:37–59
- Medvedev GS (2006) Transition to bursting via deterministic chaos. *Phys Rev Lett* 97:048102
- Medvedev GS, Yoo Y (2008) Chaos at the border of criticality. *Chaos* 18(3):033105,7
- Milik A, Szmolyan P, Löffelmann H, Gröller E (1998) Geometry of mixed-mode oscillations in the 3-d autocatalator. *Int J Bifurc Chaos* 8:505–519
- Pedersen MG, Sørensen MP (2006/07) The effect of noise in β -cell burst period. *SIAM J Appl Math* 67(2):530–542 (electronic), 2006/07
- Pontryagin LS, Rodygin LV (1960) Periodic solution of a system of ordinary differential equations with a small parameter in the terms containing the derivatives. *Sov Math Dokl* 1:611–614
- Rinzel J (1985) Bursting oscillations in an excitable membrane model. In: Sleeman BD, Jarvis RJ (eds) *Ordinary and partial differential equations*. Springer-Verlag, Berlin, pp 304–316
- Rinzel J, Troy WC (1982a) Bursting phenomena in a simplified Oregonator flow system d activity an model. *J Chem Phys* 76:1775–1789
- Rinzel J, Troy WC (1982b) A one-variable map analysis of bursting in the belousov-zhabotinskii reaction. *Lect Notes Biomath* 51:1–23
- Rubin JE (2006) Bursting induced by excitatory synaptic coupling in non-identical conditional relaxation oscillators or square-wave bursters. *Phys Rev E* 74:021917
- Rulkov NF (2002) Modeling of spiking-bursting neural behavior using two-dimensional map. *Phys Rev E* 65:041922–041930
- Rulkov NF (2004) Oscillations in large-scale cortical networks: map-based model. *J Comput Neurosci* 17:203–223
- Smith JC, Ellenberger HH, Ballay K, Richter DW, Feldman JL (1991) Pre-Bötzinger complex: a brainstem region that may generate respiratory rhythm in mammals. *Science* 254:726–729
- Su J, Rubin J, Terman D (2004) Effects of noise on elliptic bursters. *Nonlinearity* 17:133–157
- Terman D (1991) Chaotic spikes arising from a model for bursting in excitable membranes. *SIAM J Appl Math* 51:1418–1450
- Terman D (1992) The transition from bursting to continuous spiking in an excitable membrane model. *J Nonlinear Sci* 2:133–182
- The MathWorks, Inc (2008) *MATLAB The Language of Technical Computing*, version 7.6.0.324(r2008a) edition
- Wang X (1991) Period-doublings to chaos in a simple neural network. *IEEE*, pp 333–339